Journal of Materials Chemistry A

PAPER

View Article Online
View Journal | View Issue

Cite this: J. Mater. Chem. A, 2017, 5, 4114

A germanium nanoparticles/molybdenum disulphide (MoS_2) nanocomposite as a high-capacity, high-rate anode material for lithium-ion batteries†

Meng-Hsun Hsieh,‡ Guo-An Li,‡ Wei-Chung Chang and Hsing-Yu Tuan*

Received 29th September 2016
Accepted 10th January 2017

DOI: 10.1039/c6ta08455a

www.rsc.org/MaterialsA

A facile synthesis of Ge/MoS_2 nanocomposites is developed by blending Ge nanoparticles into MoS_2 nanosheets in solution at room temperature followed by annealing at 350 °C. The decoration with Ge nanoparticles in this compound can synergistically improve the electrochemical performance of LIBs because of increased conductivity and structure stability. Ge/MoS_2 nanocomposites exhibit a high reversible capacity of 1362 mA h g^{-1} cycled at 0.2 A g^{-1} after 50 cycles. Even at high rate capability (>1 A g^{-1}), the battery performance of Ge/MoS_2 from 0.2 A g^{-1} to 15 A g^{-1} is superior to the performances of the reported graphene-based and other nanoparticle-decorated MoS_2 anodes. Finally, a coin-type full-cell with a high areal capacity (~3 mA h cm^{-2}) and a high volumetric capacity (~1700 mA h cm^{-3}) was also achieved with a Ge/MoS_2 anode and a Li(MnCoNi)O_2 cathode.

Introduction

To date, rechargeable Li-ion batteries (LIBs) play an important role in powering portable electronic devices (PEDs) such as laptops, smart phones and tablets. Since the rapid development of hybrid electric vehicles (HEV) and electric vehicles (EV), LIBs with a high energy density are very much required.[1,2] LIBs with a high energy density can be achieved by replacing the traditional graphite anode with other electrode materials, which have higher capacity than graphite (372 mA h g^{-1}).[3,4]

Recently, two dimensional (2D) layered structures have attracted tremendous attention for their use in LIBs, optoelectronic devices and hydrogen evolution catalysis due to their unique properties.[5,6] Among them, layered transition-metal dichalcogenides, including MoS_2, $MoSe_2$, WS_2 and WSe_2, attract much attention due to their sandwich structure (chalcogen–metal–chalcogen). MoS_2 is a suitable candidate for replacing commercial graphite owing to its high theoretical capacity (670 mA h g^{-1}) and weak van der Waals forces between Mo and S layers. Due to the weak binding energy between the S–Mo–S layers, Li-ions can easily intercalate and de-intercalate into the layered structure.[7–9] Despite the fact that bulk MoS_2 has these advantages, the practical application of the bulk MoS_2 anode for LIBs still faces some challenges such as inferior electrochemical performance and rapid decay in capacity because of the poor electronic conductivity, and less active sites.[10,11] Therefore, considerable research efforts have been devoted to improving the above-mentioned problems of bulk MoS_2. Various nanostructures of MoS_2 like nanospheres, hollow nanospheres, nanosheets[3,12–14] and carbon-based composites[15–19] are adopted to improve the electronic conductivity, add the active sites and shorten the diffuse path of Li-ions. Nevertheless, the methods above-mentioned are usually involved in complicated manufactural procedures and under harsh reaction conditions to hamper its practical application in industries.

Currently, one feasible strategy is to design effective hybridization of two species electrochemically active anode materials as many literature studies reported.[20–25] By blending other electrochemically active constituents, synergistically improved electrochemical properties such as electrical/ionic conductivity, mechanical stability, and high energy density which are difficult to achieve in a single energy storage system were manifested. In this smart integrated composite, the electrode can absorb the volume variation of the active material during lithium insertion/removal, similar to the concept of intermetallic alloying compounds,[26–28] and host reversibly a larger amount of lithium. Meantime, electrochemical activities of individual components are fully presented, and the interface/chemical distributions are homogeneous in the nanocomposites.

Germanium (Ge) nanoparticles and nanowires have been proposed as a potential candidate for LIBs owing to their high theoretical capacity and high rate capability.[29–37] In this study,

Department of Chemical Engineering, National Tsing Hua University, 101, Section 2, Kuang-Fu Road, Hsinchu, Taiwan 30013, Republic of China. E-mail: hytuan@che.Nthu.edu.tw; Fax: +886-3-571-5408; Tel: +886-3-572-3661

† Electronic supplementary information (ESI) available: SEM images, XRD, and TEM images of MoS_2 nanosheets and Ge nanoparticles; Nyquist plots of Ge/MoS_2 nanocomposites. See DOI: 10.1039/c6ta08455a

‡ These authors contributed equally to this work.

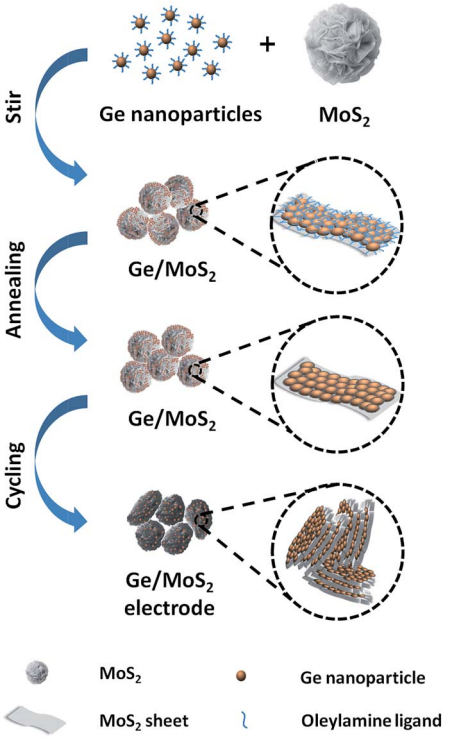

Scheme 1 Illustration of a facile process and structure evolution after cycles of the Ge/MoS_2 composites.

we developed Ge/MoS_2 composites to address the issue of high rate capability (>1 A g^{-1}) of MoS_2-based electrodes. Ge nanoparticles are introduced into the Ge/MoS_2 composites because they are favourable for high rate tests. Ge/MoS_2 nanocomposites exhibit an outstanding performance with a reversible capacity of 1362 mA h g^{-1} at 0.2 A g^{-1} after 50 cycles and high rate capability (>1 A g^{-1}). By building up the integrated architecture, there are several advantages as follows. First of all, both MoS_2 and Ge can store lithium ions so that the overall energy density of the electrode was improved with a volumetric capacity of 1700 mA h cm^{-3}, about 3 times than that of graphite.[38] Besides, structure evolution after cycles of the Ge/MoS_2 with well-distribution of Ge nanoparticles is shown in Scheme 1, which makes electrons easily transfer contributing to excellent high rate capability. In terms of germanium, the huge volume variance issue during the process is effectively tackled through the frame of the product of MoS_2 (Li_2S and Mo). In other words, the rational hybridization of MoS_2 and Ge is mutually beneficial to address their individual inherent defects in electrochemical behaviour. For practical application, the coin-type full-cell (CR2032) of Ge/MoS_2 composites as an anode and Li(MnCoNi)O_2 as a cathode had been fabricated with a high reversible areal capacity (~3 mA h cm^{-2}) and a high volumetric capacity (~1700 mA h g^{-1}) and used to power the electronic device.

Experimental section

Chemicals

All chemicals and solvents were used as received. Ammonium molybdate tetrahydrate ($(NH_4)_6Mo_7O_{24}\cdot 4H_2O$, 81.0–83.0% MoO_3 basis), thiourea (NH_2CSNH_2, 99%), germanium(II) bromide ($GeBr_2$, 97%), oleylamine (OLA, $C_{18}H_{37}N$, 70%), poly(acrylic acid) (PAA, average $M_V \sim 450\,000$), carboxymethylcellulose sodium salt (CMC, $C_{28}H_{30}Na_8O_{27}$), ethanol (C_2H_5OH, 99.8%) and toluene ($C_6H_5CH_3$, reagent grade) were purchased from Sigma-Aldrich. Lithium hexafluorophosphate ($LiPF_6$), fluoroethylene carbonate (FEC, $C_3H_3FO_3$), diethyl carbonate (DEC, $C_5H_{10}O_3$), super P carbon black, lithium metal foil, copper metal foil, Celgard membrane and coin-type cell CR2032 were purchased from Shining Energy Co., Ltd.

Synthesis of MoS_2 nanosheets

Synthesis of the MoS_2 nanosheets was based on a previous literature study.[39] In the beginning, 0.143 mmol ammonium molybdate tetrahydrate and 4.28 mmol thiourea were dissolved in 5 ml deionized water under vigorous stirring for 30 minutes. During stirring, the solution gradually became transparent. The solution was transferred to a batch reactor and heated at 180 °C for 24 h. The hot reactor was removed from the heater followed by rapid cooling to room temperature. The as-synthesized products were cleaned three times by centrifugation at 8000 rpm for 5 minutes with 5 ml deionized water and 35 ml ethanol. After the cleaning step, the products were annealed at 800 °C for 2 h under an argon atmosphere.

Synthesis of Ge nanoparticles

Ge nanoparticles were synthesized using procedures from a previous study.[40,41] In a typical synthesis, 1 mmol $GeBr_2$ and 20 ml OLA were added to a 50 ml three-necked flask in an argon-filled glovebox. After removal of the three-necked flask from the glovebox, one neck was quickly connected to the Schlenk line. Another was connected to a thermocouple for monitoring the temperature. The other was connected to a rubber septum for sealing. Then, the mixture was vigorously stirred and degassed under argon atmospheres at 120 °C for 30 minutes. After purging, the mixture was heated to 260 °C and maintained for 2 h. Finally, the black colloidal solution was formed and the flask was cooled to room temperature. By adding 5 ml of toluene and 35 ml of ethanol, the mixture was washed three times at 8000 rpm for 5 minutes. After washing, GeNPs were dispersed in toluene for further application.

Synthesis of Ge/MoS_2 composites

Ge nanoparticles and MoS_2 were mixed in a 50 ml three-necked flask with a 2 : 1 weight ratio and then OLA (15 ml) and toluene (30 ml) were also added into the three-necked flask. After the solution was vigorously stirred for 12 h at room temperature, the Ge/MoS_2 composites were obtained by centrifugation with 5 ml toluene and 35 ml ethanol at 8000 rpm for 5 minutes for three times. Moreover, unnecessary oleylamine ligands, which can result in poor electrical conductivity, on the surface of Ge nanoparticles were eliminated by heating to 350 °C for 2 h in a furnace under an argon atmosphere. After annealing, the Ge/MoS_2 composites were collected and applied to the following characterization and electrochemical tests.

Lithium ion battery assembly

80 wt% active materials (Ge/MoS_2), 10 wt% super-p carbon black, 5 wt% PAA and 5 wt% CMC were mixed in ethanol and deionized water to form a homogeneous slurry, which was tape-cast on a copper foil and dried in an oven to fabricate the electrode of Ge/MoS_2. Before assembling, the electrode was dried at 150 °C for 2 h under an argon atmosphere to remove the residual water. The coin-type half-cell (CR2032), which contained 0.5 mg Ge/MoS_2 composites electrodes, a lithium metal foil and a PP/PE/PP membrane soaked in an electrolyte, was assembled in an argon-filled glovebox. The electrolyte consisted of 1 M $LiPF_6$ in a mixture of fluoroethylene carbonate/diethyl carbonate (FEC/DEC) (3 : 7 v/v). For the coin-type full-cell (CR2032), $Li(MnCoNi)O_2$ was used as a cathode instead of the lithium metal and the Ge/MoS_2 composite was used as an anode.

Electrochemical characterization

All materials were characterized by field emission scanning electron microscopy (FESEM), transmission electron microscopy (TEM), high-resolution transmission electron microscopy (HRTEM) and X-ray diffraction (XRD). For SEM imaging, images were characterized by using a FESEM (HITACHI-SU8010) at an accelerating voltage of 10–15 kV with an 8 mm working distance. The TEM samples were prepared by dispersing the powder in ethanol and drop-casting onto a carbon-coated copper grid. The TEM and HRTEM images were acquired by using an accelerating voltage of 200 kV with a Philips TECNAI 20 and an accelerating voltage of 300 kV with a JEOL JEM-3000F, respectively. XRD patterns were recorded by using a Shimadzu XRD-6000 diffractometer, which was equipped with CuK radiation.

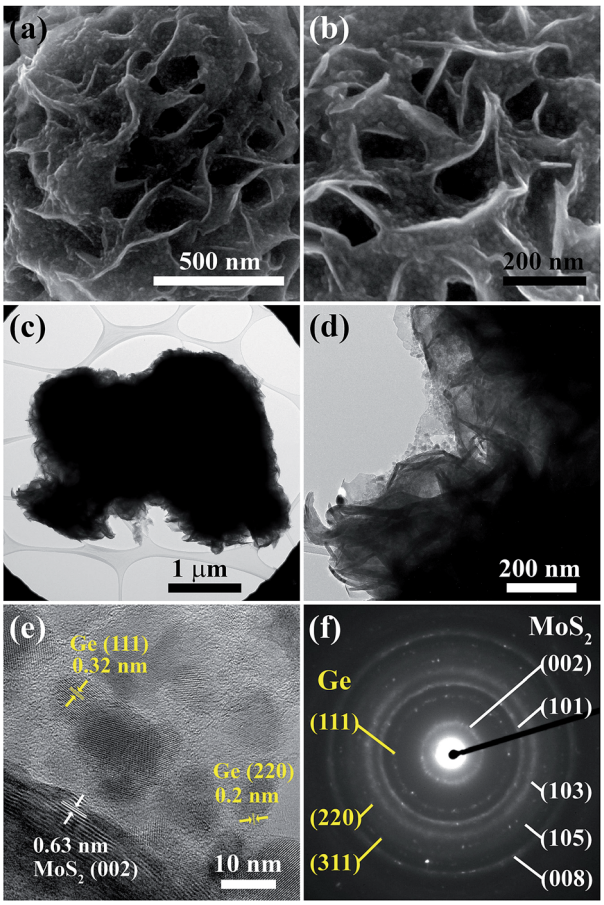

Fig. 1 (a and b) SEM images, (c and d) TEM images, (e) HRTEM image and (f) SAED pattern of the Ge/MoS_2 composites prepared by mixing Ge nanoparticles and MoS_2 nanosheets at room temperature.

Results and discussion

The Ge/MoS_2 nanocomposites were prepared by mixing the as-synthesized Ge nanoparticles and the as-synthesized MoS_2 for 12 h at room temperature. The SEM images of the Ge/MoS_2 composites are shown in Fig. 1(a and b). Obviously, the MoS_2 nanosheets were densely covered by a large amount of Ge nanoparticles. In Fig. 1(c and d), the low-magnification and high-magnification TEM images of the Ge/MoS_2 composites clearly show the overall shape, which is composed of abundant Ge nanoparticles and MoS_2 nanosheets. In addition, the HRTEM image of the Ge/MoS_2 composites in Fig. 1(e) shows that the obvious interplanar spacing of the Ge and the MoS_2 corresponds to the (111) and (220) crystalline planes of Ge and the (002) crystalline plane of MoS_2, respectively. The SAED pattern of the Ge/MoS_2 composites in Fig. 1(f) clearly exhibits the different ring patterns, which are consistent with the (111), (220) and (311) crystalline planes of Ge and the (002), (101), (103), (105) and (008) crystalline planes of MoS_2.

To remove the unnecessary oleylamine ligands, the Ge/MoS_2 composites were annealed at 350 °C for 2 h under an argon atmosphere. Herein, the Ge/MoS_2 composites, which are not specially mentioned, indicate that the composites had undergone the annealing process. The morphology of the Ge/MoS_2 composites is still unchanged as shown in Fig. 2(a and b) in comparison with the one of Ge/MoS_2 composites before annealing in Fig. 1(a and b). A high density of Ge nanoparticles are uniformly scattered on the MoS_2 nanosheets. TEM images of the Ge/MoS_2 composites in Fig. 2(c and d) also maintain the same morphology like the Ge/MoS_2 composites before annealing in Fig. 1(c and d). SEM and TEM images in Fig. 2(a–d) prove that the annealing process cannot cause any change of structure. Energy-dispersive spectroscopy (EDS) elemental mappings of the Ge/MoS_2 composites clearly show the homogeneous distribution of the Mo, S and Ge elements (red, green and yellow represent the elements of Mo, S and Ge, respectively) as shown in Fig. 2(e and f). Moreover, the HRTEM image of the Ge/MoS_2 composites in Fig. 2(g) clearly shows the interplanar spacing, which is 0.32 nm and 0.63 nm, corresponding to the (111) crystalline plane of the Ge and the (002) crystalline plane of the MoS_2, respectively. The SAED pattern of the Ge/MoS_2 composites in Fig. 2(h) shows several rings, which are consistent with the ring patterns of Ge/MoS_2 composites before annealing as shown in Fig. 1(f). According to the XRD patterns of the Ge/MoS_2 composites before and after annealing in Fig. 3, both of them are similar and are indexed to the JCPDS database of

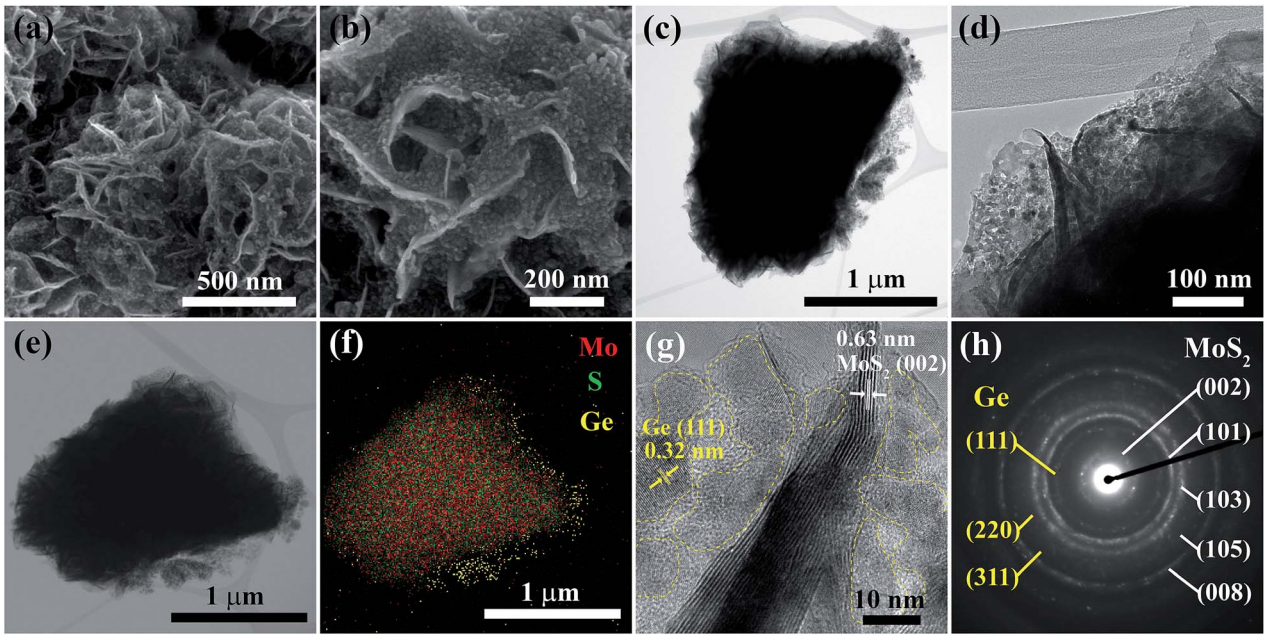

Fig. 2 (a and b) SEM images, (c and d) TEM images, (e and f) EDS elemental mappings (Mo (red), S (green) and Ge (yellow)), (g) HRTEM image, and (h) SAED pattern of the annealed Ge/MoS_2 nanocomposites.

the Ge (#895011) and the MoS_2 (#371492). From the result of interplanar spacing, SAED and XRD patterns, the composites still maintain the original phase after the annealing process.

Galvanostatic cycling performance of the Ge/MoS_2 composites with a current density at 0.2 A g^{-1} is shown in Fig. 4(a). In the beginning, the current density at 0.1 A g^{-1} was used to form a dense solid electrolyte interfere (SEI) layer. The first discharge and charge specific capacities are 1600 and 1282 mA h g^{-1}, corresponding to a nearly 80% coulombic efficiency. The irreversible capacity was mainly caused by forming a SEI layer on the electrode during the first discharge and charge process. After the first cycle, the subsequent cycles show a high reversible capacity without apparent fading after 50 cycles. The 50th cycle exhibits that the specific capacity of charge is 1362 mA h g^{-1}, which maintains a nearly 100% charge capacity of the 2nd cycle.

The voltage profile of the Ge/MoS_2 composites in Fig. 4(b) exhibits several potential plateaus observed in the first discharge (lithiation) process at 1.1, 0.6–0.7 and 0.1–0.5 V and in the first charge (delithiation) process at 2.2 and 0.4–0.6 V. In the following cycles, the plateaus can be observed at 2 and 0.1–0.2 V in the discharge process and at 2.2–2.3 and 0.5 V in the charge process. Fig. 4(c) shows the differential capacity curves at various cycles, including the 1st, 10th and 20th cycle. The peaks indicate the lithiation and delithiation of the composite. In the first discharge cycle, the sharp peak at 1.1 V is the formation of Li_xMoS_2 and the broad peak at 0.6–0.7 V is the reaction of Li_xMoS_2 to metallic molybdenum (Mo) and Li_2S through conversion reactions based on the previous studies.[22,42] Meanwhile, the broad peak at 0.6–0.7 V is probably attributed to the formation of the SEI layer from electrochemical reduction of the electrolyte. The SEI reaction, which occurs at nearly 0.6 V, will disappear after forming a passivating SEI layer on the surface of the electrode.[43] The other peaks at the first discharge cycle between 0.1 and 0.5 V are the formation of the various Li–Ge alloy phases according to the literature.[30,32,34] In the first charge cycle, the peaks evident upon 2.2 V and 0.4–0.6 V is the delithiation of Li_2S and Li–Ge alloys, respectively. For the following discharge cycles, the main peaks appear on nearly 2 V and 0.1–0.2 V corresponding to lithiation of S and Ge, respectively. The peaks in the following charge cycles (2.2–2.3 V and 0.5 V) are related to the delithiation of Li_2S and Li–Ge alloys.

In summary, MoS_2 in the composite irreversibly uptakes lithium ions at first and then decomposes into Mo and Li_2S through conversion reactions around at 0.6 V. During lithium intercalation, germanium itself reversibly forms an alloy with lithium. While in the discharge process, the molybdenum and lithium disulfide were oxidized near a potential of 2.2 V. For the following cycles, the reaction with lithium for the Ge/MoS_2 composite includes conversion reactions and alloying reactions (Ge alloy/dealloy reaction) as described as follows.

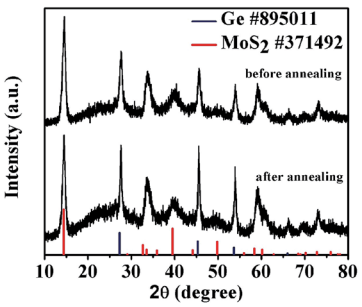

Fig. 3 XRD patterns of the Ge/MoS_2 composites before and after annealing.

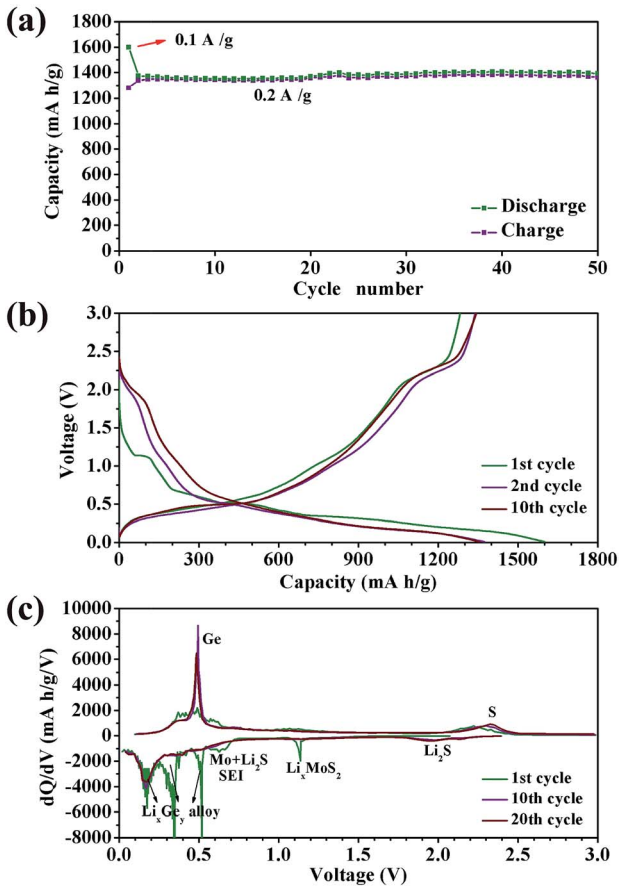

Fig. 4 (a) Cycling performance of the Ge/MoS_2 composites at a rate of 0.1 A g^{-1} for the initial cycle and following cycles at a rate of 0.2 A g^{-1}. (b) Voltage profiles of the Ge/MoS_2 composites at 1st, 2nd and 10th cycle. (c) Differential capacity curves of the Ge/MoS_2 composites at 1st, 10th and 20th cycle.

$$MoS_2 + xLi \rightarrow Li_xMoS_2 \rightarrow Mo + 2L_2S\ (\sim 0.6\ V\ vs.\ Li/Li^+)$$

$$Mo + Li_2S \leftrightarrow 2Li + S + Mo\ (\sim 2.2\ V\ vs.\ Li/Li^+)$$

$$Ge + xLi \leftrightarrow Li_xGe\ (\sim 0.3\ V\ vs.\ Li/Li^+)$$

The Ge/MoS_2 composites have to be examined by various current densities. Fig. 5(a) shows the rate capability of the Ge/MoS_2 composites in a wide range of current density from 0.1 to 15 A g^{-1} and the current density at 0.1 A g^{-1} was only used in the first cycle. Then, all of the discharge and charge current densities were kept the same. The first discharge and charge specific capacities are 1524 mA h g^{-1} and 1213 mA h g^{-1}, respectively. In the rate capability test, the Ge/MoS_2 composites exhibit that the average specific capacity of charge is 1306 (0.2 A g^{-1}), 1247 (0.5 A g^{-1}), 1169 (1 A g^{-1}), 1064 (2 A g^{-1}), 958 (3 A g^{-1}), 790 (5 A g^{-1}), 658 (7 A g^{-1}), 511 (10 A g^{-1}) and 333 (15 A g^{-1}) mA h g^{-1}, respectively. After Ge/MoS_2 composites were tested at different current densities, the rate was quickly returned to 0.2 A g^{-1} for 10 cycles and the average charge capacity is nearly equivalent to the initial average capacity (1306 mA h g^{-1}) at 0.2 A g^{-1}.

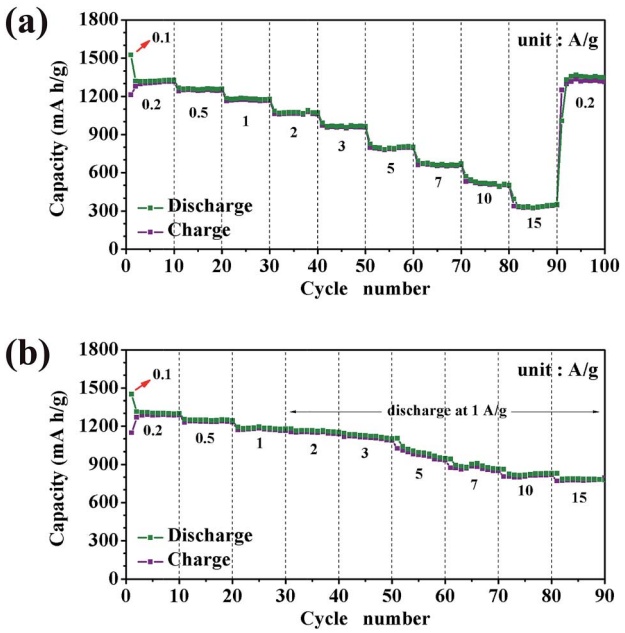

Fig. 5 Rate capability of the Ge/MoS_2 composites from 0.1 to 15 A g^{-1}. (a) All of the discharge rates are equal to the charge rates. (b) Discharge and charge at low rates (0.1, 0.2, 0.5 and 1 A g^{-1}) are kept the same and the discharge rate is fixed to 1 A g^{-1} at high charge rates (2, 3, 5, 7, 10 and 15 A g^{-1}).

The rate capability of the Ge/MoS_2 composites was also evaluated from 0.1 to 15 A g^{-1} in Fig. 5(b). Under the experimental conditions, the current density of discharge and charge at 0.1, 0.2, 0.5 and 1 A g^{-1} is maintained the same. In addition, the current density of charge is changed to 2, 3, 5, 7, 10 and 15 A g^{-1} with the fixed discharge rate (1 A g^{-1}). For the first cycle (0.1 A g^{-1}), the discharge and charge capacities are 1451 and 1147 mA h g^{-1}, respectively. The average charge capacity of the Ge/MoS_2 composites is 1285 mA h g^{-1} (0.2 A g^{-1}), 1235 mA h g^{-1} (0.5 A g^{-1}), 1172 mA h g^{-1} (1 A g^{-1}), 1147 mA h g^{-1} (2 A g^{-1}), 1106 mA h g^{-1} (3 A g^{-1}), 974 mA h g^{-1} (5 A g^{-1}), 867 mA h g^{-1} (7 A g^{-1}), 809 mA h g^{-1} (10 A g^{-1}) and 777 mA h g^{-1} (15 A g^{-1}), respectively. To prove the effect of hybridization of two active anode materials, the rate capability of bare MoS_2 was determined and is shown in Fig. S7.† Under a variety of current densities including 0.1C, 0.5C, 1C, 2C, 3C, 5C, 7C, 10C, and back to 0.1C (1C = 1A g^{-1}), the first cycle charge/discharge capacity of bare MoS_2 is 943 mA h g^{-1} and 821 mA h g^{-1}, respectively, showing a coulombic efficiency of 87%. Capacity decreased swiftly over cycles at 0.5C, and even worse results at higher rates from 1C to 10C were obtained, implying poor conductivity of bare MoS_2 nanosheets. Besides, the composite with excess Ge nanoparticles was blended to show poor electrochemical performance as depicted in Fig. S8(b).† Theoretically, the rate performance will be increased as the amount of Ge nanoparticles increases. We speculate that the situation is probably caused by nanoparticle aggregation during the cycling process. All the results clearly demonstrate the excellent cycling stability and rate capability of the as-prepared Ge/MoS_2 electrode.

Performance and stability at high rates (>1 A g^{-1}) are significant challenges for the MoS_2-based anode due to the effects of low electrical conductivity of the MoS_2 nanosheets. The galvanostatic discharge/charge cycles are tested with the current density at 5 and 7 A g^{-1}. As shown in Fig. 6(a), the cycling performance of the Ge/MoS_2 composites shows high stability and reversible capacity at 5 A g^{-1}. For the first cycle, the current density at 0.1 A g^{-1} is used and the discharge and charge capacities are 1481 and 1175 mA h g^{-1} with a nearly 79% coulombic efficiency. After 100 cycles, the Ge/MoS_2 composites still exhibit high stability and reversible capacity. Then, the average charge capacity at 5 A g^{-1} is approximately 790 mA h g^{-1}. Fig. 6(b) shows the capacity of the Ge/MoS_2 composites with a higher current density at 7 A g^{-1} and the average charge capacity is nearly 594 mA h g^{-1}. After 100 cycles, the Ge/MoS_2 composites also show good stability and capacity. The insets of Fig. 6(a and b) present the voltage profile of the Ge/MoS_2 composites at 1st, 10th and 100th cycles and the potential plateaus are similar to the above result with the current density at 0.2 A g^{-1} in Fig. 4(b).

The structure evolution of the Ge/MoS_2 composites with a current density at 7 A g^{-1} after 100 cycles is shown in Fig. 7(a). After galvanostatic discharge and charge cycles for 100 cycles, the Ge/MoS_2 composites exhibit an agglomerate structure, which will cause a fast fading in capacity due to the decreasing active sites. However, superior performance and stability of the Ge/MoS_2 composites can be attributed to the Ge nanoparticles, which act as spaces in the agglomerate structure to make the electrode accessible for the penetration of the electrolyte. EDS

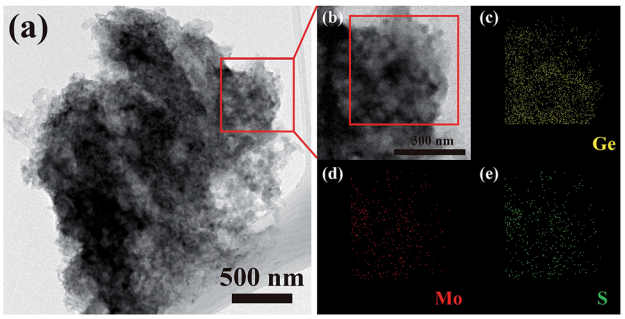

Fig. 7 (a) Structure evolution and (b–e) EDS elemental mappings of the Ge/MoS_2 composites with a current density at 7 A g^{-1} after 100 cycles.

elemental mappings of the Ge/MoS_2 composites after 100 cycles are shown in Fig. 7(b–e). Obviously, elements of Ge (yellow), Mo (red) and S (green) are uniformly dispersed in the agglomerate. In particular, homogeneous distribution of Ge nanoparticles can play an important role in stabilizing the structure and preventing the restack. Due to the stable and integrated structure, Ge/MoS_2 composites exhibit superior cycling performance.

To verify the feasibility of the Ge/MoS_2 composites for practical application, the coin-type full-cell (CR2032) was assembled with a Ge/MoS_2 anode and a Li(MnCoNi)O_2 cathode. As shown in Fig. 8(a), the cycling performance of the coin-type full-cell with a current density at 0.3 A cm^{-2} for 30 cycles is nearly 3 mA h cm^{-2}. From Fig. 8(a), the volumetric capacity of the Ge/MoS_2 electrode was also calculated around 1700 mA h cm^{-3} (thickness of the Ge/MoS_2 electrode is nearly 18 μm) which is at least five times higher than that of the commercial graphite (330–430 mA h cm^{-3}).[44] High volumetric capacity can effectively reduce the volume of the anode and enhance the energy density based on the

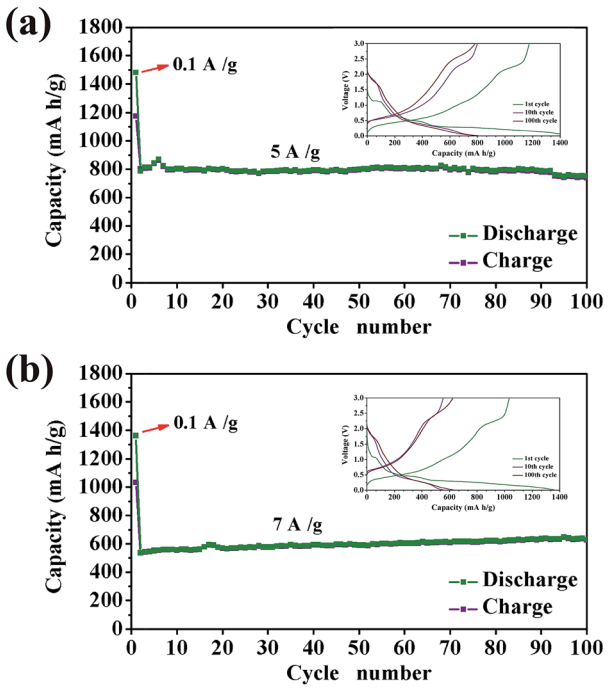

Fig. 6 Galvanostatic discharge and charge cycles between 0.01 and 3 V of the Ge/MoS_2 composites. The current density at 0.1 A g^{-1} for the first cycle followed by a rate of (a) 5 A g^{-1} and (b) 7 A g^{-1} for total 100 cycles. The insets in (a) and (b) show the voltage profile at 1st, 10th and 100th cycles.

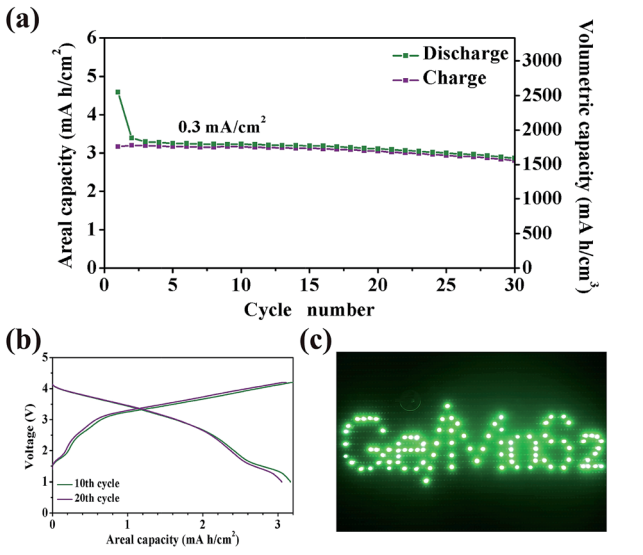

Fig. 8 (a) Areal and volumetric capacity of coin-type full-cell (CR2032) with a Ge/MoS_2 anode and a Li(MnCoNi)O_2 cathode with current density at 0.3 A cm^{-2} for 30 cycles. (b) Voltage profile of the coin-type full-cell with current density at 0.3 A cm^{-2} at 10th and 20th cycles. (c) Coin-type full-cell was used to power the green LEDs (87 bulbs).

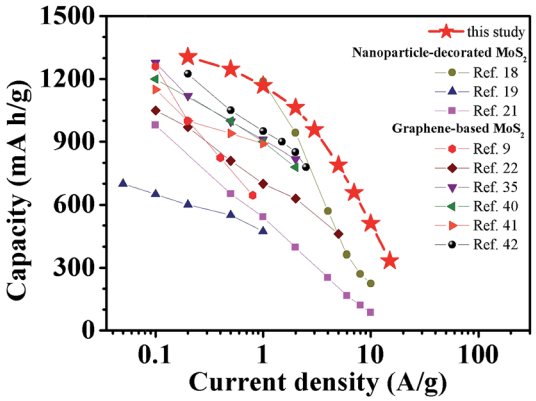

Fig. 9 Cycling performance of the Ge/MoS_2 anode in comparison with those of the studies about graphene-based and nanoparticle-decorated MoS_2. The red star symbolizes our data, which were calculated based on the active material, from 0.2 to 15 A g^{-1} (discharge and charge rates were kept the same).

same volume. The voltage profile of the coin-type full-cell at 10th and 20th cycle shown in Fig. 8(b) exhibits several potential plateaus during the discharge and charge cycles. In the discharge process (lithiation of the Ge/MoS_2 composites), potential plateaus at 1.5–3.2 V are contributed by the MoS_2. On the other hand, potential plateaus at 3.2–4.2 V are attributed to the reaction of the Ge nanoparticles. In the charge process (delithiation of the Ge/MoS_2 composites), the voltage curve at 1–2.5 V and at 2.5–4.2 V is the reaction of the MoS_2 and Ge, respectively. For further application, the coin-type full-cell had been used to power a LED board with the green LED (87 bulbs), which displays the words "Ge/MoS_2" in Fig. 8(c).

Conclusions

In summary, Ge/MoS_2 composites with densely covered Ge nanoparticles on MoS_2 nanosheets were successfully synthesized through a mixing process. By a series of electrochemical tests, Ge/MoS_2 composites deliver superior cycling performance, reversible capacity and rate capability. Ge nanoparticles successfully prevent the restack of the structure and effectively enhance the specific capacity at high rates (>1 A g^{-1}). In Fig. 9, Ge/MoS_2 composites show superior battery performance from 0.2 A g^{-1} to 15 A g^{-1} (discharge and charge rates were kept the same) in comparison with those in the previous studies based on graphene-based[11,45–49] and nanoparticle-decorated MoS_2.[50–52] Excellent performance can be attributed to a robust structure, which consisted of Ge nanoparticles and MoS_2 nanosheets. In this structure, Ge nanoparticles act as the spacers to effectively prevent the restack of MoS_2 nanosheets and make the adjacent MoS_2 nanosheets accessible to the electrolyte. Moreover, high areal capacity and high volumetric capacity of full cells have been achieved, which are critical for practical applications.

Acknowledgements

The authors acknowledge the financial support by the Ministry of Science and Technology of Taiwan (NSC 102-2221-E-007-023-MY3, NSC 102-2221-E-007-090-MY2, NSC 101-2623-E-007-013-IT, and NSC 102-2633-M-007-002), the Ministry of Economic Affairs, Taiwan (101-EC-17-A-09-S1-198), and National Tsing Hua University (102N2051E1).

Notes and references

1 N. Nitta and G. Yushin, *Part. Part. Syst. Charact.*, 2014, **31**, 317–336.
2 V. Etacheri, R. Marom, R. Elazari, G. Salitra and D. Aurbach, *Energy Environ. Sci.*, 2011, **4**, 3243–3262.
3 X. F. Qian, Y. R. Wang, W. Zhou, L. P. Zhang, G. S. Song and S. Q. Cheng, *Int. J. Electrochem. Sci.*, 2015, **10**, 3510–3517.
4 K. C. Klavetter, J. P. de Souza, A. Heller and C. B. Mullins, *J. Mater. Chem. A*, 2015, **3**, 5829–5834.
5 F. Xiong, H. T. Wang, X. G. Liu, J. Sun, M. Brongersma, E. Pop and Y. Cui, *Nano Lett.*, 2015, **15**, 6777–6784.
6 K. N. Zhao, L. Zhang, R. Xia, Y. F. Dong, W. W. Xu, C. J. Niu, L. He, M. Y. Yan, L. B. Qu and L. Q. Mai, *Small*, 2016, **12**, 588–594.
7 G. D. Du, Z. P. Guo, S. Q. Wang, R. Zeng, Z. X. Chen and H. K. Liu, *Chem. Commun.*, 2010, **46**, 1106–1108.
8 R. T. Lv, J. A. Robinson, R. E. Schaak, D. Sun, Y. F. Sun, T. E. Mallouk and M. Terrones, *Acc. Chem. Res.*, 2015, **48**, 897.
9 T. Stephenson, Z. Li, B. Olsen and D. Mitlin, *Energy Environ. Sci.*, 2014, **7**, 209–231.
10 U. K. Sen and S. Mitra, *ACS Appl. Mater. Interfaces*, 2013, **5**, 1240–1247.
11 G. H. Yuan, G. Wang, H. Wang and J. T. Bai, 2016, **660**, 62–72.
12 S. P. Zhang, B. V. R. Chowdari, Z. Y. Wen, J. Jin and J. H. Yang, *ACS Nano*, 2015, **9**, 12464–12472.
13 J. B. Ding, Y. Zhou, Y. G. Li, S. J. Guo and X. Q. Huang, *Chem. Mater.*, 2016, **28**, 2074–2080.
14 Y. Wang, L. Yu and X. W. Lou, *Angew. Chem., Int. Ed.*, 2016, **55**, 7423–7426.
15 Y. C. Liu, Y. P. Zhao, L. F. Jiao and J. Chen, *J. Mater. Chem. A*, 2014, **2**, 13109–13115.
16 S. Hu, W. Chen, J. Zhou, F. Yin, E. Uchaker, Q. F. Zhang and G. Z. Cao, *J. Mater. Chem. A*, 2014, **2**, 7862–7872.
17 X. Li, J. Y. Zhang, R. Wang, H. Y. Huang, C. Xie, Z. H. Li, J. Li and C. M. Niu, *Nano Lett.*, 2015, **15**, 5268–5272.
18 L. F. Jiang, B. H. Lin, X. M. Li, X. F. Song, H. Xia, L. Li and H. B. Zeng, *ACS Appl. Mater. Interfaces*, 2016, **8**, 2680–2687.
19 Y. Liu, X. He, D. Hanlon, A. Harvey, U. Khan, Y. Li and J. N. Coleman, *ACS Nano*, 2016, **10**, 5980–5990.
20 B. A. Chen, E. Z. Liu, F. He, C. S. Shi, C. N. He, J. J. Li and N. Q. Zhao, *Nano Energy*, 2016, **26**, 541–549.
21 X. Xu, Z. Y. Fan, S. J. Ding, D. M. Yu and Y. P. Du, *Nanoscale*, 2014, **6**, 5245–5250.
22 B. J. Guo, K. Yu, H. Fu, Q. Q. Hua, R. J. Qi, H. L. Li, H. L. Song, S. Guo and Z. Q. Zhu, *J. Mater. Chem. A*, 2015, **3**, 6392–6401.
23 Y. G. Huang, Q. C. Pan, H. Q. Wang, C. Ji, X. M. Wu, Z. Q. He and Q. Y. Li, *J. Mater. Chem. A*, 2016, **4**, 7185–7189.
24 L. Qiao, X. H. Wang, L. Qiao, X. L. Sun, X. W. Li, Y. X. Zheng and D. Y. He, *Nanoscale*, 2013, **5**, 3037–3042.

25 Q. Q. Xiong, J. P. Tu, X. H. Xia, X. Y. Zhao, C. D. Gu and X. L. Wang, *Nanoscale*, 2013, **5**, 7906–7912.
26 J. O. Besenhard, J. Yang and M. Winter, *J. Power Sources*, 1997, **68**, 87–90.
27 M. Winter and J. O. Besenhard, *Electrochim. Acta*, 1999, **45**, 31–50.
28 D. Bresser, S. Passerini and B. Scrosati, *Energy Environ. Sci.*, 2016, **9**, 3348–3367.
29 C. O'Regan, S. Biswas, N. Petkov and J. D. Holmes, *J. Mater. Chem. C*, 2014, **2**, 14–33.
30 F. W. Yuan, H. J. Yang and H. Y. Tuan, *ACS Nano*, 2012, **6**, 9932–9942.
31 P. R. Abel, K. C. Klavetter, K. Jarvis, A. Heller and C. B. Mullins, *J. Mater. Chem. A*, 2014, **2**, 19011–19018.
32 T. Kennedy, E. Mullane, H. Geaney, M. Osiak, C. O'Dwyer and K. M. Ryan, *Nano Lett.*, 2014, **14**, 716–723.
33 J. Hwang, C. Jo, M. G. Kim, J. Chun, E. Lim, S. Kim, S. Jeong, Y. Kim and J. Lee, *ACS Nano*, 2015, **9**, 5299–5309.
34 F. W. Yuan and H. Y. Tuan, *Chem. Mater.*, 2014, **26**, 2172–2179.
35 S. Fang, L. F. Shen, H. Zheng and X. G. Zhang, *J. Mater. Chem. A*, 2015, **3**, 1498–1503.
36 T. Kennedy, M. Bezuidenhout, K. Palaniappan, K. Stokes, M. Brandon and K. M. Ryan, *ACS Nano*, 2015, **9**, 7456–7465.
37 L. Q. Mai, X. C. Tian, X. Xu, L. Chang and L. Xu, *Chem. Rev.*, 2014, **114**, 11828–11862.
38 J. Y. Liu, X. Chen, J. Kim, Q. Y. Zheng, H. L. Ning, P. C. Sun, X. J. Huang, J. H. Liu, J. J. Niu and P. V. Braun, *Nano Lett.*, 2016, **16**, 4501–4507.
39 J. F. Xie, J. J. Zhang, S. Li, F. Grote, X. D. Zhang, H. Zhang, R. X. Wang, Y. Lei, B. C. Pan and Y. Xie, *J.Am. Chem. Soc.*, 2013, **135**, 17881–17888.
40 X. M. Lu, B. A. Korgel and K. P. Johnston, *Chem. Mater.*, 2005, **17**, 6479–6485.
41 D. J. Xue, J. J. Wang, Y. Q. Wang, S. Xin, Y. G. Guo and L. J. Wan, *Adv. Mater.*, 2011, **23**, 3704–3707.
42 S. J. Ding, D. Y. Zhang, J. S. Chen and X. W. Lou, *Nanoscale*, 2012, **4**, 95–98.
43 J. X. Guo, H. F. Zhu, Y. F. Sun, L. Tang and X. Zhang, *J. Mater. Chem. A*, 2016, **4**, 4783–4789.
44 N. Nitta, F. X. Wu, J. T. Lee and G. Yushin, *Mater. Today*, 2015, **18**, 252–264.
45 Y. Wang, B. Chen, D. H. Seo, Z. J. Han, J. I. Wong, K. Ostrikov, H. Zhang and H. Y. Yang, *NPG Asia Mater.*, 2016, **8**, e268.
46 C. Y. Zhao, X. Wang, J. H. Kong, J. M. Ang, P. S. Lee, Z. L. Liu and X. H. Lu, *ACS Appl. Mater. Interfaces*, 2016, **8**, 2372–2379.
47 L. Jiang, B. Lin, X. Li, X. Song, H. Xia, L. Li and H. Zeng, *ACS Appl. Mater. Interfaces*, 2016, **8**, 2680–2687.
48 H. L. Li, K. Yu, H. Fu, B. J. Guo, X. Lei and Z. Q. Zhu, *J. Phys. Chem. C*, 2015, **119**, 7959–7968.
49 F. Y. Xiong, Z. Y. Cai, L. B. Qu, P. F. Zhang, Z. F. Yuan, O. K. Asare, W. W. Xu, C. Lin and L. Q. Mai, *ACS Appl. Mater. Interfaces*, 2015, **7**, 12625–12630.
50 Y. Chen, J. Lu, S. Wen, L. Lu and J. M. Xue, *J. Mater. Chem. A*, 2014, **2**, 17857–17866.
51 Y. Chen, B. H. Song, X. S. Tang, L. Lu and J. M. Xue, *Small*, 2014, **10**, 1536–1543.
52 X. Q. Zhu, C. Yang, F. Xiao, J. D. Wang and X. T. Su, *New J. Chem.*, 2015, **39**, 683–688.